39

Data-Based Modeling of the Earth's Magnetic Field

Nikolai Tsyganenko[1], Varvara Andreeva[1], Marina Kubyshkina[1], Mikhail Sitnov[2], and Grant Stephens[2]

ABSTRACT

This chapter addresses the empirical models of the terrestrial magnetosphere based on large amounts of spacecraft data from many past and present satellite missions. Unlike computer simulations, which derive the expected magnetospheric configurations by solving first-principle equations, the data-based models seek to reconstruct the real-world magnetosphere from direct in situ observations and, in that sense, represent the "ground truth" of the data. The empirical models are based on three cornerstones: multiyear archives of satellite and ground data, a mathematical framework describing the magnetospheric field sources, and parametrization methods relating the model input to the solar wind drivers and/or ground-based geomagnetic indices. Accordingly, this chapter includes three sections devoted to each of the above aspects. In conclusion, we discuss future prospects and challenges, with a particular focus on reconstructing instantaneous real-time magnetospheric configurations, based on simultaneous data of multisatellite constellations of the geospace monitors.

39.1. INTRODUCTION

The geomagnetic field is widely known to serve as a giant umbrella protecting our planet from space radiation. In solar–terrestrial studies, it is also considered as a principal agent connecting the ionosphere with the solar corona and playing a principal role in space weather phenomena. Unlike meteorological conditions in the atmosphere, the space weather and the environment it impacts cannot be directly seen and felt. Its forecasting relies on satellite data scattered in time and space and on sophisticated computer simulations that solve first-principle equations of physics. The problem is complicated by the extreme variability of the distant geomagnetic field and widely different scenarios of the interplanetary input.

Before the space era, empirical models of the geomagnetic field were limited to its main part generated by sources inside Earth, and relied mostly on ground observations. Since the launch of the first satellite in 1957, rapid outward expansion of space exploration resulted in a huge and ever-growing wealth of archived data, covering now more than four solar cycles. The main approach adopted in early models was to combine the data with indirect knowledge based on a *priori* assumptions derived from theory. At present, the plentiful amount of historical data ensures a sufficiently dense coverage both in the geometric and parametric space. This allows us to reduce the preconceived notions about the models' architecture, increase their flexibility and resolution, and maximize information extracted from the data. This chapter overviews the history of empirical magnetosphere models, outlines basic principles of their construction, and highlights recent progress, largely based on the authors' works.

[1]*Institute and Department of Physics, Saint-Petersburg State University, Saint-Petersburg, Russia*

[2]*Johns Hopkins University Applied Physics Laboratory, Laurel, MD, USA*

Space Physics and Aeronomy Collection Volume 2: Magnetospheres in the Solar System, Geophysical Monograph 259, First Edition. Edited by Romain Maggiolo, Nicolas André, Hiroshi Hasegawa, and Daniel T. Welling.

DOI: 10.1002/9781119815624.ch39

39.2. DATA FOR EMPIRICAL MODELING

Geospace magnetometer data, combined with concurrent interplanetary and ground-based observations, are a cornerstone of the empirical magnetosphere modeling. Mead and Fairfield (1975) compiled the first set of such data collected by four IMP missions between 1966 and 1972 and used it to create the *MF75* model. Tsyganenko and Usmanov (1982) added HEOS-1 and -2 data to the Mead–Fairfield set and developed a more realistic *TU82* model with explicitly defined equatorial currents. The data set was further extended by adding ISEE-1 and -2 data (Fairfield et al., 1994); the unified database covered the period 1966–1986 and was utilized in the derivation of the widely used *T89* and *T96* models (Tsyganenko, 1989a, 1995, 1996).

In the following years, the launch of AMPTE/CCE/IRM (1984), Geotail (1992), Wind (1994), Polar (1996), ACE (1997), Cluster (2001), Themis (2007), Van Allen Space Probes (2012), MMS (2015), and the series of geosynchronous GOES satellites resulted in rapid and continuing expansion of the data pool. The abundance of data was instrumental to improve the models' accuracy, critically dependent on the data coverage in the geometric and parametric space. Note that storm-time observations, most interesting for space weather studies, constitute only a small part of the entire database; this issue will be addressed in more detail in section 39.2.2. In terms of the spatial origin, three kinds of data are used in the modeling: (1) spacecraft data taken inside the magnetosphere, (2) ground activity indices such as Kp, Sym-H, or AE, and (3) upstream data of solar wind monitors, used to parameterize the model field response to the external driving.

39.2.1. Data Resolution Issues

At low altitudes, spacecraft speed can reach several km s^{-1}, while a typical scale of local field sources (e.g., thickness of Birkeland current layers) is a few hundred kilometers, which puts an upper limit of ~1 minute on the data resolution needed to properly resolve the magnetic structures at altitudes of 2–3R_E. In the distant magnetosphere, by contrast, using such fine resolution is superfluous, resulting in unreasonably large files with largely redundant data. The optimal choice here is to use five-minute averaging intervals, which corresponds to a ~20 R_E travel distance of the solar wind around the magnetosphere, commensurate with its transverse scale size. This can also be justified from the viewpoint of interplanetary data, most of which come from upstream monitors at the L1 libration point and, hence, must be delayed in time by $\Delta T \sim$ 40–60 minutes. As demonstrated by Mailyan et al. (2008), even the best of existing methods to estimate ΔT are accurate to only 5–10 minutes. Given the added uncertainties in the magnetospheric response timescales, the five-minute resolution is more than sufficient for the interplanetary data.

39.2.2. Data Preparation

Due to a variety of raw data formats, the first procedure is to reformat the files by merging the magnetic field and satellite ephemeris vectors, and transform them into a suitable coordinate system (usually GSE). In the inner magnetosphere, the main geomagnetic field rapidly rises with decreasing distance, so that even small inaccuracies in the satellite position and orientation can result in large errors in the external field. Note that, while a spacecraft position is known with high precision, the angular orientation data are much less accurate (except in the case of dedicated low-altitude missions such as Magsat, SWARM, and CHAMP). This issue becomes important at low altitudes where, in addition, the onboard magnetometers are switched into a high-range operation mode. As a result, data taken at near-perigee distances $r \leq$ 3–4 R_E are often useless for the modeling purposes. Since the solar wind frequently deviates from strictly radial direction, the modeling results are generally better organized in the solar-wind-magnetospheric (GSW) coordinates (Tsyganenko et al., 1998) incorporating the "windsock" effect. The relevant transformations are performed using the solar wind aberration angles, calculated from the observed flow velocity components.

An important factor affecting the modeling accuracy is the uniformity of data distribution in the geometric and parametric space. This is illustrated in Figure 39.1, showing meridional (top) and equatorial (bottom) plots of the columnar density of observations in the "grand" database, used in the construction of recent models (Tsyganenko and Andreeva, 2015, 2016, 2017, 2018b). The database includes in total almost five million records, provided by observations onboard Geotail, Polar, Cluster, Themis, and Van Allen space probes from 1996 to 2016. Naturally, the most densely populated region is the inner equatorial magnetosphere, where Van Allen, Polar, and Themis-A, -D, and -E missions were the main contributors. At larger distance, the coverage density is significantly lower, especially in the tail lobes; most of the data in those regions came from Geotail and Cluster; also, note the outstanding gap at distances from ~30 to ~50 R_E.

In terms of the parametric coverage, the most important factor is the disturbance level, directly related to the intensity of external driving by geoeffective solar wind streams. This issue is crucial to the models' ability to reproduce space weather impact on the magnetosphere.- Figure 39.2 shows the occurrence frequency of data as functions of Sym-H and of the normalized N-index by

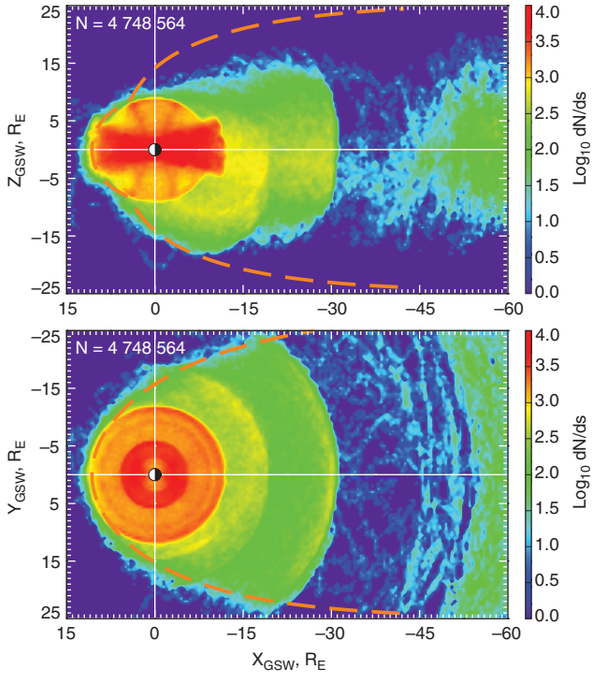

Figure 39.1 Distribution of data in the "grand" database of space magnetometer data: (top) in the noon–midnight meridian and (bottom) equatorial planes. The color-coded quantity is the logarithm of the column-integrated number of data records, falling into 0.5 × 0.5RE coordinate intervals. Average magnetopause position is shown by red dashed line.

Newell et al. (2007): $N = 10^{-4} V^{4/3} B_{\perp}^{2/3} \left(\sin \frac{\theta_c}{2} \right)^{8/3}$, where V, $B_{\perp}$, and θ_c are the solar wind speed, the IMF transverse component, and clock angle, respectively. The N-index quantifies the IMF merging rate at the magnetopause and is directly related to the electromagnetic energy intake into the geospace. The shaded areas lie between the 5th and 95th percentiles and correspond to mostly quiet and weakly disturbed conditions.

The dominance of undisturbed data and the dramatic falloff of the histograms toward lower Sym-H and higher N values demonstrate the rapidly dropping probability of space weather events with increasingly stronger intensity. To properly model the most interesting phenomena, two possible methods can be envisaged. The first one is to compile smaller subsets containing only data from selected events of interest, as in the TS05 model (Tsyganenko and Sitnov, 2005) based on 37 storm events. Alternatively, one can assign a weight to each data record, inversely proportional to the data density at a given location in the parametric space. Such a method was used in the *TS07D* (Tsyganenko and Sitnov, 2007) and *TA15* (Tsyganenko and Andreeva, 2015) models.

39.3. MATHEMATICAL STRUCTURE OF EMPIRICAL MODELS

The starting point in creating any empirical magnetosphere model is to represent the total magnetic field as the sum of the field $\mathbf{B}_{int}$ due to the internal sources and of the external field $\mathbf{B}_{ext}$ associated with currents flowing

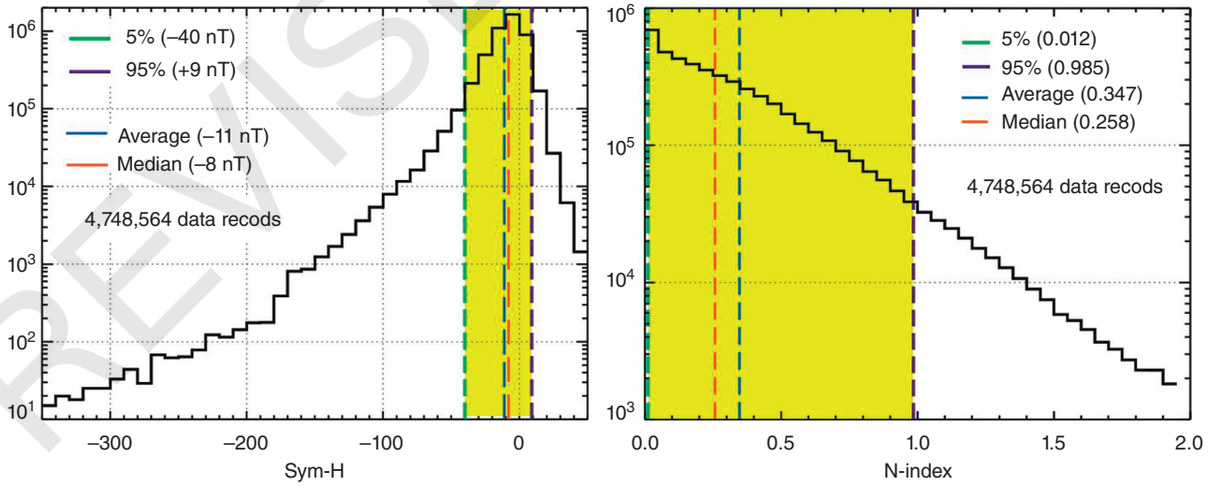

Figure 39.2 Histograms of the data distribution with respect to Sym-H index (left) and normalized N-index (right). Note the log scale on the vertical axes. Average and median values, as well as 5%, and 95% boundaries are shown by vertical dashed lines according to the legend. The shaded areas contain 90% of the data (between the 5th, and 95th percentiles).

in the ionosphere and above. The internal field is assumed to be known with high accuracy from standard IGRF models (Thébault et al., 2015), regularly updated every five years. This chapter focuses exclusively on the modeling of the external component $\mathbf{B}_{ext}$.

The horizontal ionospheric currents flow within a relatively thin layer at altitudes of 90–150 km, where their magnetic effect never exceeds a few percentage of the total field. At larger distances it rapidly becomes negligible and does not affect the field line shape. For that reason, the ionospheric sources are commonly ignored in the distant field models.

At the very beginning of the space era, the modeling was based on very limited amounts of in *situ* data, without any knowledge of the concurrent state of the interplanetary medium. For that reason, the earliest models relied solely on the modular principle, based on representing the field $\mathbf{B}_{ext}$ as a sum of a few vector functions, corresponding to a few principal current systems. Geometry of the field sources was prescribed *a priori* on the basis of simple theoretical arguments and very limited data, while the space weather impact on the magnetosphere was modeled by binning the data into a few intervals of ground activity indices.

As an alternative to the modular method, the external field can be represented by expansions into sums of formal basis functions, unrelated to the actual structure of the field sources. Thus, Mead and Fairfield (1975) expanded the field components in powers of coordinates; similar mathematical forms were also employed by Ostapenko and Maltsev (1997). Interest in that approach surged in the recent decade (Tsyganenko and Sitnov, 2007; Sitnov et al., 2008, 2010, 2017, 2018; Stephens et al., 2013, 2016, 2019; Andreeva and Tsyganenko, 2016, 2018; Tsyganenko and Andreeva, 2016, 2017, 2018a, 2018b), inspired by the dramatically improved coverage of the magnetosphere by contemporary observations.

39.3.1. The Modular Models

In the modular models, the external field $\mathbf{B}_{ext}$ is represented as a sum of partial fields associated with principal current systems (Figure 39.3):

$$\mathbf{B}_{ext} = \mathbf{B}_{RC} + \mathbf{B}_{TC} + \mathbf{B}_{FAC} + \mathbf{B}_{MP} + \mathbf{B}_{P} \qquad (39.1)$$

including the ring (RC), tail (TC), field-aligned (FAC), and the magnetopause (MP) currents; the latter's role is to confine (shield) the total field inside the magnetopause. Because of the reconnection between the magnetospheric and interplanetary magnetic field (IMF), the shielding is not perfect, which is taken into account by the empirical "penetration" term $\mathbf{B}_P$, usually represented as a fraction of the IMF. In the following sections we discuss in more detail each term in the right-hand side of equation (39.1).

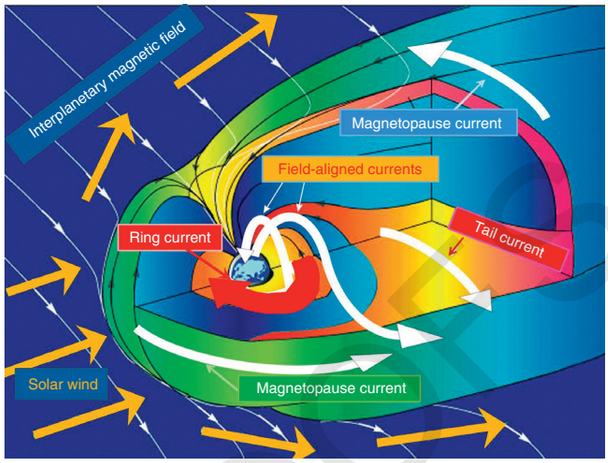

Figure 39.3 Overview of the magnetospheric large-scale electric current systems (courtesy M. Fujimoto, JAXA).

Equation (39.1) does not include the effect of cusp currents due to the diamagnetism of injected magnetosheath plasma. The cusp currents are concentrated within a limited MLT sector around noon and produce cleft-like magnetic field depressions, protruding inward from the high-latitude dayside magnetopause. None of the existing empirical models properly describe the cusp magnetic effects; we address them in more detail in section 39.3.3.

The Ring Current Module. Historically, the ring current (RC) was the first known large-scale extraterrestrial source of the geomagnetic field, discovered at the dawn of the space age. It resides closest to Earth in a region with strong quasi-dipolar geomagnetic field, which made it a relatively easy target for early studies based on the drift approximation (Akasofu and Chapman, 1961).

Data-based modeling of the RC magnetic effects began with a study by Olson and Pfitzer (1974) who fitted a wire model to scalar data of OGO-3/5 satellites. A compact empirical RC representation, based on a modification of the dipolar vector potential, entered as a component in the data-based *TU82* and *T87* models (Tsyganenko and Usmanov, 1982; Tsyganenko, 1987), fitted to magnetometer data of IMP, HEOS, and ISEE missions. In a subsequent *T96* model (Tsyganenko, 1995, 1996; Tsyganenko and Stern, 1996), a more realistic RC was introduced, based on a combination of equatorial current disks (Tsyganenko and Peredo, 1994) with variable thickness and flexible radial profiles of the current density.

The early models, however, shared a common deficiency: the axial symmetry. In reality, the outer RC is asymmetric in both the noon–midnight and dawn–dusk directions, especially during space storms, when a strong partial ring current (PRC) develops in the dusk sector,

accompanied by the increase of associated Region 2 FACs. The problem inevitably becomes three-dimensional, which greatly complicates its mathematical treatment.

A possible solution is to reconstruct the electric current system from observed radial profiles of plasma pressure, using a simple model of the inner geomagnetic field (Roelof, 1989; Stern, 1993; Tsyganenko, 1993). Figure 39.4 (Tsyganenko, 2014) illustrates a sample SRC/PRC configuration, derived from anisotropic plasma pressures $P_\perp$ (r_e) and $P_\parallel$ (r_e) (Lui and Hamilton, 1992) and azimuthally asymmetric magnetic field (*T89* +dipole) by calculating the drift, magnetization, and field-aligned currents from standard equations (Rossi and Olbert, 1970, Chapter 9.4).

The main challenge, however, is not to obtain the currents, but to derive from them a compact and numerically fast magnetic field module. A feasible two-step solution (Tsyganenko, 2000) is to first derive a "target" field $\mathbf{B}_t$ by Biot–Savart summation over a dense set of points. Then a simple analytical starting field $\mathbf{B}_s$ is devised, subject to a flexible deformation $\hat{\mathbf{T}}$, such that the deformed field $\mathbf{B}_{\rm mod} = \hat{\mathbf{T}} \cdot \mathbf{B}_s$ fits as close as possible to the target field $\mathbf{B}_t$. That approach is essentially based on the deformation technique (Stern, 1987; Tsyganenko, 1998a), a powerful tool often used in the empirical modeling. Thus obtained symmetric (SRC) and partial (PRC) modules are entered in *T02* (Tsyganenko, 2002a, 2002b) and *TS05* (Tsyganenko and Sitnov, 2005) models, as well as in the most recent *TA15* model (Tsyganenko and Andreeva, 2015).

The Tail Field Module. Geometrically, the TC is the simplest current system. Early crude models (see a review by Roederer, 1969) represented it by a uniform thin sheet unbounded in the dawn–dusk direction. Subsequent investigations (Tsyganenko and Usmanov, 1982; Tsyganenko, 1987, 1989a) sought to develop more realistic representations of the TC field, including a finite TC thickness, flow line curvature, tailward decrease of the current density, TC warping due to the dipole tilt, and its twisting caused by the IMF B_y. The results were implemented in the *TU82, T87,* and *T89* empirical models, representing the magnetospheric field at different activity levels. The most widely used *T89* model was based on compact axisymmetric solutions of Ampere's equation for the vector potential, corresponding to an infinitely thin current sheet with a simple radial profile of the current density $J(\rho)$:

$$\nabla \times \nabla \times \mathbf{A}(\rho, z) = \mu_0 J(\rho)\delta(z)\mathbf{e}_\phi \qquad (39.2)$$

Subsequent development of that method (Tsyganenko and Peredo, 1994) yielded more flexible representations of the TC field, used in a popular *T96* model (Tsyganenko, 1995, 1996), and in the following *T02* (Tsyganenko, 2002a, 2002b) and *TS05* (Tsyganenko and Sitnov, 2005) models. A major step in that direction (Tsyganenko and Sitnov, 2007) was to lift the assumption of axial symmetry and find a solution of Ampere's equation in the form of Fourier–Bessel integral, subsequently converted into an expansion over a discrete set of wavenumbers. This approach is addressed in more detail in section 39.3.2.

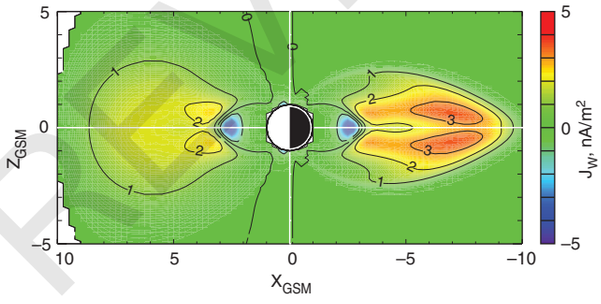

Figure 39.4 Noon–midnight distribution of westward component of electric current volume density, derived from a bell-shaped plasma pressure profile by Lui and Hamilton (1992) and a noon–midnight asymmetric magnetic field, a sum of *T89* and dipole field (after Tsyganenko, 2014).

Field-Aligned Current Module. The field-aligned (Birkeland) currents were first discovered at low altitudes (Zmuda and Armstrong, 1974; Iijima and Potemra, 1976), but it was soon realized that they extend much farther from Earth and form a global system, fundamentally important from at least two viewpoints. First, the Region 1 (R1) FACs form the outermost system that directly connects the solar-wind driven generator in the magnetosheath with the high-latitude ionosphere. Second, in terms of global magnetospheric geometry, the R1 FACs are inherently associated with the magnetic shear in the transition region between the closed quasi-dipolar field in the inner magnetosphere and the higher-latitude field, swept tailward due to the magnetized solar wind flow. In this section we address only the R1 field modeling, since the R2 currents constitute an intrinsic part of the PRC, already discussed in section 39.3.1.1.

The greatest difficulty in the modeling of the R1 FAC is the lack of a theory elucidating their geometry in the distant magnetosphere. While the R2 FACs can be at least roughly evaluated from simple plasma pressure and magnetic field models, the only way to empirically reconstruct the R1 FAC system is to start from their known distribution at low altitudes, assume a quasidipolar shape of the FAC flow lines at intermediate locations, but to largely

rely on guesswork and/or use MHD simulations to define them in the distant magnetosphere.

Efforts to model the FAC magnetic effects on large-scale data date from at least quarter century ago (Tsyganenko, 1991; *Stern,* 1993). The former work (Tsyganenko, 1991) focused on the R1 field and used a simple model with radial currents flowing in a conical layer, crossing the ionosphere along the R1 FAC oval. The disturbance field was represented via a simple vector potential and fairly well reproduced observations by LEO satellites. The conical model failed, however, at higher altitudes, where the FACs are not rectilinear but flow along quasi-dipolar lines.

In a subsequent study (Tsyganenko, 2000), a more realistic model was developed, with the FAC layer shape represented in spherical SM coordinates $\{r, \theta, \phi\}$ as a single funnel-like flared surface:

$$\theta(r,\phi) = \arcsin\left[\frac{\sqrt{r}}{\left(r^{\nu} + \sin^{-2\nu}\theta_{o}(\phi) - 1\right)^{1/2\nu}}\right] \qquad (39.3)$$

where $\theta_o(\phi)$ defines the colatitude of the funnel's base (hence, the FAC oval size and shape) at the ionospheric altitude.

A unique property of surfaces defined by equation 39.3 is that their meridional sections and the FAC flow lines are close to dipolar L-shells at low altitudes, but gradually open outward and, asymptotically, flatten out parallel to the equatorial plane at large distances. The variable parameter ν quantifies the surface flaring rate, so that for larger values of ν the transition from dipole-like to nearly planar shape occurs at lower latitudes. Being rather compact and flexible, the representation 39.3 has been used since then in several models.

The azimuthal variation of FAC density on the surface (equation (39.3)) was assumed in the simplest form of Fourier harmonics as $I(\phi) \sim \sin m\phi$ or $\sim \cos m\phi$, with the magnitude coefficients to be found from data. The above described model of the FAC sheet has been adopted in all recent modular models, including *T02, TS05, TS07D,* and *TA15*. Figure 39.5 illustrates the global 3-D geometry of the model Region 1 FAC system based on equation 39.3.

As already noted, defining the electric current is only the first step: it still remains to devise a computationally efficient magnetic field representation, which is a more involved task. Until recently, the basic strategy adopted to construct the FAC module in the *T02, TS05,* and *TS07D* models was the same as in the SRC/PRC case, outlined in section 39.3.1.1. Namely, the first step was to create a target set of field vectors by Biot–Savart summation over the entire current layer. Subsequently, a simple conical model of the starting field and its flexible deformation were defined, and their parameters were jointly fitted to minimize the r.m.s. difference between the model and target fields.

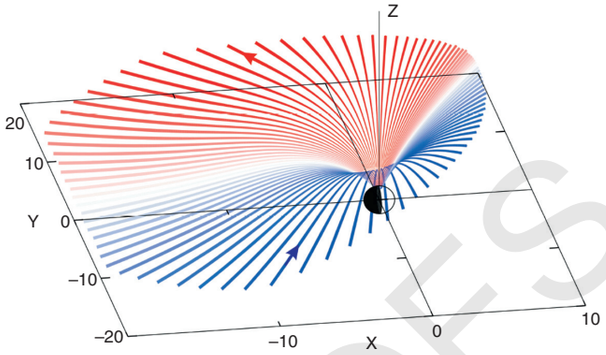

Figure 39.5 Large-scale configuration of the model R1 FAC flow lines as described by equation (39.3). Blue/red lines in the morning/evening sectors correspond to downward/upward currents, respectively. Only the northern half of the entire system is displayed. At large distances the currents close via the magnetopause (not shown).

While the above method adequately represents the global magnetic field of FACs, it is not free from drawbacks. First, the deformation procedure is cumbersome and the resulting model lacks flexibility. It also works fairly well only for the lowest first and second longitude harmonics, but rapidly deteriorates for higher order terms, which does not allow the modeling of azimuthally localized near-noon currents associated with northward IMF, often termed in the literature as "Region 0" FACs. In addition, using the conical model as a starting field excludes from the outset the azimuthal FAC component; in particular, this rules out the closure of distant R1 FACs across the midnight meridian. Last, but not least, the deformation technique ensures $\nabla \cdot \mathbf{B} = 0$, but cannot control $\nabla \times \mathbf{B}$, which results in significant unphysical currents in the case of large dipole tilt angles.

In view of the above, in the most recent models, starting with *TA15,* the FAC module was constructed using a different, more transparent and flexible approach. Instead of building the model field by deformations, the magnetic field is derived from a vector potential obtained by Biot–Savart summation over electric current flow lines lying on the surface (equation (39.3)). The summation is simplified by replacing small volume elements of the FAC tube with a set of straight segments with linearly varying half-thickness, which finally yields the magnetic field components in a closed and computationally tractable form.

As in the earlier models, the R1 FAC density in *TA15* was assumed to vary with the solar-magnetic longitude ϕ in the simplest form $\sim \sin\phi$, implying dawn–dusk symmetry with zero currents at noon. In actuality, the dayside

FAC configuration is more complex (Laundal et al., 2018; Tenfjord et al., 2015), with a significant latitudinal splitting and azimuthal overlapping of prenoon and postnoon segments of the FAC oval, controlled by the magnitude and polarity of the IMF B_y. These effects have been taken into account in a generalized model proposed in a more recent study (Tsyganenko and Andreeva, 2018b). Even though the data used in that work came from magnetospheric missions and did not include low-altitude observations, the polar diagrams of FAC density (Figure 39.6) agree well with those reconstructed from AMPERE data based on LEO Iridium satellites, as well as with the MHD-simulated FAC maps (Korth et al., 2010, 2011).

Magnetopause and the Modular Shielding Principle. A fundamental feature of the solar wind–magnetosphere interaction is that the geomagnetic flux is confined inside the magnetopause. In early models (Mead and Beard, 1964) a total confinement, or shielding, was assumed, which implied no connection between the interplanetary and geomagnetic fields across the boundary. In reality, the IMF partially penetrates inside the magnetosphere, which is accounted for by the separate term $\mathbf{B}_P$ in equation (39.1).

Contributions from all field sources, including the Earth's field $\mathbf{B}_{int}$, $\mathbf{B}_{RC}$, $\mathbf{B}_{TC}$, and $\mathbf{B}_{FAC}$ are assumed from the outset to be fully shielded by the potential field $\mathbf{B}_{MP}$ inside a prescribed boundary. In principle, the shielding field $\mathbf{B}_{MP}$ can be uniquely determined, once the total field from all intramagnetospheric sources is known. However, the terms $\mathbf{B}_{int}$, $\mathbf{B}_{RC}$, $\mathbf{B}_{TC}$, and $\mathbf{B}_{FAC}$ must represent not just a single state but many a *priori* unknown configurations, corresponding to different magnetospheric conditions. With this in mind, each of the above modules is split into a linear combination of several submodules with unknown magnitude coefficients and nonlinear parameters. To ensure that the total field remains shielded for any combination of the coefficients, the shielding term $\mathbf{B}_{MP}$ is also expanded into a sum of partial terms, entering in pairs with the corresponding intramagnetospheric field terms (Tsyganenko, 1995, 2013), such that the most general final form of equation (39.1) becomes:

$$\begin{aligned}\mathbf{B}_{ext} = \mathbf{B}_{MP}^{(int)} &+ \sum_i a_i^{(RC)}\left(\mathbf{b}_{RC,i} + \mathbf{h}_{MP,i}^{(RC)}\right) \\ &+ \sum_k a_k^{(TC)}\left(\mathbf{b}_{TC,k} + \mathbf{h}_{MP,k}^{(TC)}\right) \\ &+ \sum_l a_l^{(FAC)}\left(\mathbf{b}_{FAC,l} + \mathbf{h}_{MP,l}^{(FAC)}\right) + a_P\mathbf{B}_\perp^{IMF} \quad (39.4)\end{aligned}$$

Each term in the sums contains a normalized field $\mathbf{b}$ of an intramagnetospheric source, paired with its own shielding field $\mathbf{h}$ and, hence, separately meets the shielding condition at the magnetopause S:

$$(\mathbf{b} + \mathbf{h}) \cdot \mathbf{n}|_S = 0 \qquad 39.5$$

The main advantage of this approach is that it makes it possible to independently vary the parameters of individual magnetospheric field sources and, at the same time, keep the total field fully shielded inside S for any combination of the magnitude coefficients $\{a\}$.

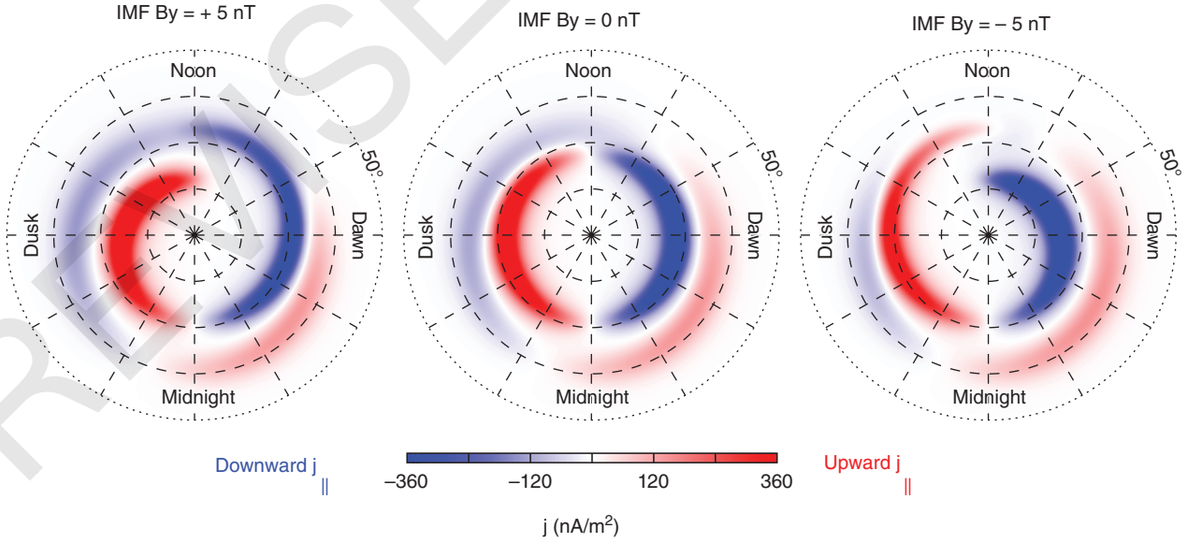

Figure 39.6 Diagrams of the model FAC density at ionospheric level for three values of IMF B_y component and negative IMF B_z (after Tsyganenko and Andreeva, 2018b). The plots demonstrate the latitudinal splitting and azimuthal overlapping of the R1 FAC near-noon segments.

The first term $\mathbf{B}_{\mathrm{MP}}^{(\mathrm{int})}$ in the right-hand side of equation 39.4, also known as the Chapman–Ferraro field, shields the Earth's main field $\mathbf{B}_{\mathrm{int}}$. Since the magnetopause is located far from Earth, all higher order harmonics in the IGRF expansion are relatively small there, which allows calculation of the shielding field using a purely dipolar approximation for $\mathbf{B}_{\mathrm{int}}$. As a result, the shielding field $\mathbf{B}_{\mathrm{MP}}^{\mathrm{int}}$ becomes independent of universal time and is controlled only by the dipole tilt angle and solar wind parameters that define the size and shape of the model magnetopause.

Since the magnetopause currents are confined to the boundary, the partial shielding fields **h** entering in equations (39.4) and (39.5) are curl-free and, hence, each of them can be represented as gradient of a scalar potential U. In early models, a traditional approach was to represent the magnetopause with a suitable analytical surface: either a paraboloid (Alekseev and Shabansky, 1972; Stern, 1985) or an ellipsoid of revolution (Tsyganenko, 1989b), or a composite spherocylindrical surface (Voigt, 1973), and find the shielding field as a solution of Neumann's problem in the form of eigenfunction expansions.

A more universal technique was introduced later, based on a seminal idea by Schulz and McNab (1987). Its essence was to replace the strict boundary condition in equation (39.5) with a weaker one, satisfied only in the r.m.s. sense. This allowed all limitations on the magnetopause shape to be lifted and, instead of the extremely limited choice between a few second-order surfaces, use a variety of analytically and/or numerically defined boundaries, such as the popular magnetopause models by Shue et al. (1998) and Lin et al. (2010). Moreover, the new method made it possible to choose the shielding potentials from a multitude of analytical solutions. The approach was first implemented in the *T96* model, where the shielding potentials were composed of cylindrical and so-called "box" harmonics: $\exp\left[x\left(p_i^2 + p_k^2\right)^{1/2}\right]\cos(p_i y)\sin(p_k z)$, derived from Laplace's equation in Cartesian coordinates.

39.3.2. The TS07D-Type Models with Higher-Resolution Equatorial Sources

In more recent works (Tsyganenko and Sitnov, 2007; Sitnov et al., 2008) a new approach was conceived and successfully implemented (Sitnov et al., 2010, 2017, 2018; Stephens et al., 2013, 2016, 2019) based on expanding the contributions from all equatorial field sources, represented by the terms $\mathbf{b}_{\mathrm{RC,i}}$ and $\mathbf{b}_{\mathrm{TC,i}}$ in equation (39.4), into a series of quasi-orthogonal basis functions. Such a generalization of the model, referred to as *TS07D,* made it possible to reveal in more detail the 2-D structure of the equatorial currents and, combined with a "nearest neighbor" data selection (see section 39.4.4), allowed the magnetospheric dynamics to be reconstructed during individual events.

The model expansions were derived by solving Ampere's equation for the vector potential of a planar current sheet:

$$\nabla \times \nabla \times \mathbf{A}(\rho,\phi,z) = \mu_0\left[\, j_\rho(\rho,\phi)\mathbf{e}_\rho + j_\phi(\rho,\phi)\mathbf{e}_\phi\right]\delta(z) \tag{39.6}$$

The above equation is a generalization of equation (39.2) to the axially asymmetric case, now including both radial and azimuthal components of the electric current density. Its solution can be derived as an expansion into a series of Fourier–Bessel terms:

$$\mathbf{A}(\rho,\phi,z) = \sum_{n=1}^{N} a_{0n}\mathbf{A}_0(k_n,\rho,z) + \sum_{m=1}^{M}\sum_{n=1}^{N} a_{mn}\mathbf{A}_m(k_n,\rho,\phi,z) \tag{39.7}$$

where the axisymmetric part of the potential is singled out into a separate sum and $k_n = n/\rho_0$, with ρ_0 being a radial scale corresponding to the largest wavelength k_1^{-1}. The summation limits, N and M, define the radial and azimuthal resolution of the model, respectively. A key feature here is a large number of quasi-orthogonal equatorial field sources, whose magnitudes a_{mn} are found by fitting the model field to data. Most recent versions of the *TS07D* model include typically a few hundred of such elementary submodules. Theoretically, the model's resolution can be made as high as needed; in reality it is restricted by the available degree of detail, depending on the data coverage of the modeled region. Note that each partial field in the expansion should be individually confined within a common boundary; to that end, the shielding field coefficients are separately computed prior to the fitting the global model to data.

39.3.3. "Magnifying Glass" Approach: RBF and BBF Models

The *TS07D* approach effectively takes advantage of the nearly two-dimensional geometry of the equatorial current sheet and, as such, cannot be extended to include in the same way the higher-latitude sources, such as the large-scale FACs and the cusp currents. In a series of recent works (Andreeva and Tsyganenko, 2016, 2018; Tsyganenko and Andreeva, 2016, 2017, 2018a, 2018b) first attempts were made to overcome that limitation and extend the "tunable resolution" concept to all three dimensions. The starting point was to represent the external field as a sum of toroidal and poloidal components (Wolf-Gladrow, 1987):

$$\mathbf{B}_{ext} = \nabla \times (\Psi_1 \mathbf{r}) + \nabla \times \nabla \times (\Psi_2 \mathbf{r}) = \nabla\Psi_1 \times \mathbf{r} + \nabla \times (\nabla\Psi_2 \times \mathbf{r}) \quad (39.8)$$

As a sum of two curls, the thus defined field is automatically divergenceless, regardless of the specific form of the scalar generating functions $\Psi_1(\mathbf{r})$ and $\Psi_2(\mathbf{r})$. The representation equation 39.8 has already been explored in the past (Kosik, 1989) as a possible way to build a magnetospheric field model, with the functions $\Psi_1(\mathbf{r})$ and $\Psi_2(\mathbf{r})$ being represented by spherical harmonics. Andreeva and Tsyganenko (2016) proposed instead to represent both generating potentials as linear combinations:

$$\Psi_{1,2}(\mathbf{r}) = \sum_{i=1}^{N} a_{i_{1,2}} \chi(|\mathbf{r} - \mathbf{R}_i|) \quad (39.9)$$

of the radial basis functions (RBF) χ, which depend only on the radial distance between the observation point and the corresponding node $\mathbf{R_i}$ of a regular 3D grid. The coefficients $a_{i_{1,2}}$ are free parameters quantifying contributions to $\mathbf{B}_{\text{ext}}$ from individual RBF nodes; their values are calculated by fitting the model equations (39.8) and (39.9) to observations. An advantage of this approach is its flexibility, achieved by placing a sufficient number of the nodes. Another benefit is the possibility to locally adjust the density of RBF centers to improve the fit quality in specific regions. In this regard, the RBF approach can be likened to a magnifying glass with adjustable focal distance and the ability to shift its field of view to different areas.

Figure 39.7 (Andreeva and Tsyganenko, 2016) shows equatorial plots of the difference $\Delta B = |\mathbf{B}_{\text{RBF}} + \mathbf{B}_{\text{dip}}| - |\mathbf{B}_{\text{dip}}|$ between the magnitudes of the total model field and of only its dipole part, obtained by fitting the RBF model to data subsets, corresponding to quiet conditions (left) and to the peak of main phase of a moderate storm (right).

The quiet-time diagram reveals a generally weak and mostly dawn–dusk symmetric external field. In a sharp contrast, the storm-time ΔB is much stronger and dramatically asymmetric, such that the inner field depression tightly envelops Earth from postmidnight through late postnoon MLT hours. The depression peaks in the premidnight sector at geocentric distances $3 \le r \le 4\ R_E$, where $\Delta B \sim -135$ nT.

In the most recent study along these lines (Tsyganenko and Andreeva, 2018a), a completely different way to define the basis source functions has been explored. Instead of expanding the global field into the toroidal and poloidal parts, a 3-D set of fully local magnetic field sources is introduced from the outset. Each source in the system is a result of applying a local radial stretch to the initially uniform field, such that the total field is represented by an ensemble of magnetic "bubbles" centered on the nodes of a 3-D grid, similar to that used in the RBF models. Using the bubble basis functions (BBF for short; not to be confused with the "Bursty Bulk Flow" abbreviation) was found to yield lower r.m.s. residuals and more regular electric currents than in the RBF models, derived from identical data sets.

Figure 39.8 presents a result of using BBF expansions to represent the magnetic depression inside the dayside cusps due to plasma diamagnetism. The left panel shows a noon–midnight meridional distribution of scalar

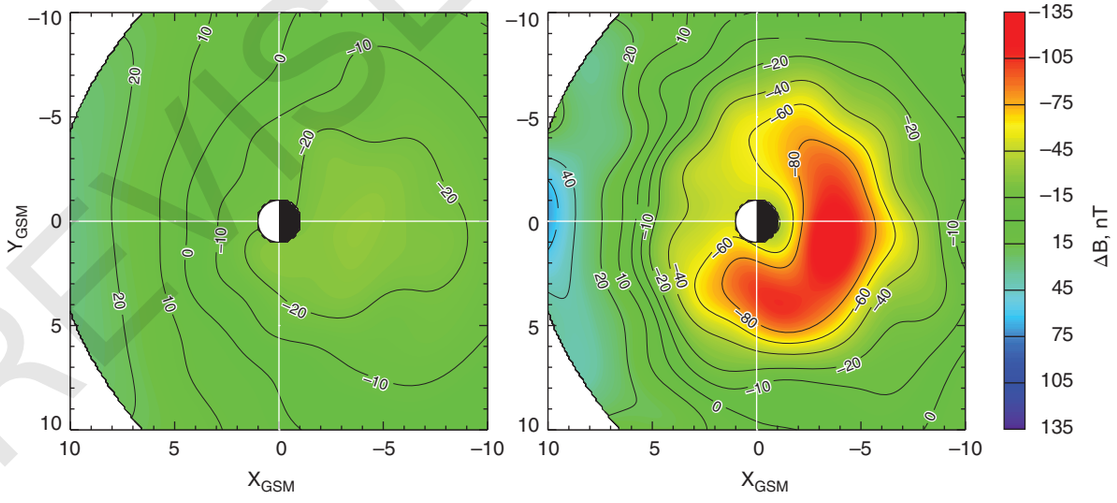

Figure 39.7 Equatorial distribution of the scalar difference $\Delta B = |\mathbf{B}_{\text{RBF}} + \mathbf{B}_{\text{dip}}| - |\mathbf{B}_{\text{dip}}|$. Positive (blue) and negative (red) values of ΔB indicate areas of compressed and depressed magnetic field, respectively. The left and right panels correspond, respectively, to quiet conditions and to the main phase peak of a moderate storm (after Andreeva and Tsyganenko, 2016).

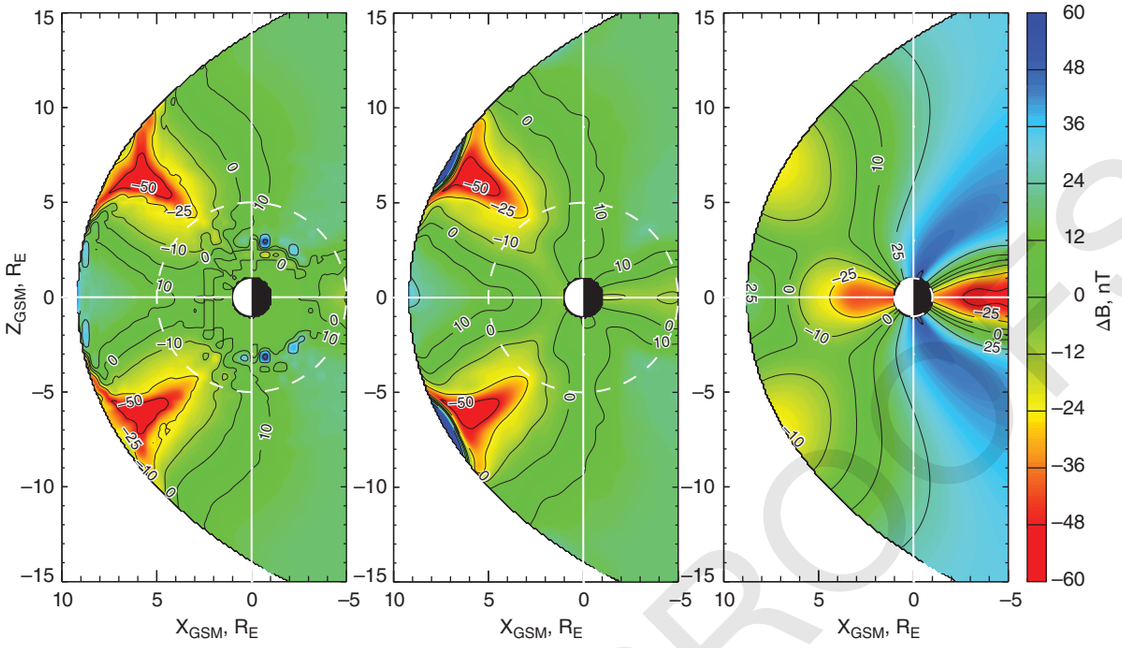

Figure 39.8 Meridional distributions of $\Delta B = |\mathbf{B}| - |\mathbf{B}_{dip}|$ in the simulated (left) and model (center) magnetosphere, represented by the BBF expansions (Tsyganenko and Andreeva, 2018a). Regions of compressed and depressed field are displayed with blue and red, respectively. For comparison, a similar plot for the *TS05* model is shown in the right panel.

difference $\Delta B = |\mathbf{B}_{BBF} + \mathbf{B}_{dip}| - |\mathbf{B}_{dip}|$, obtained from an MHD simulation run, while the center panel shows a result of fitting a BBF-based model to the artificial "data" generated in that simulation. For the reader's orientation, both distributions are clipped on the left by a model magnetopause by Lin et al. (2010) without cusp indentations.

The inner boundary of the modeling region is delineated with white dashed circle $r = 5\ R_E$. Both simulated and model distributions are very similar, except at the outermost cusp funnel boundary, where the model ΔB is overestimated due to fringe effects.

The depressions protrude inside the magnetosphere down to $r \sim 4\ R_E$, in line with previous studies (Tsyganenko and Russell, 1999; Tsyganenko, 2009; Andreeva and Tsyganenko, 2016). For comparison, the right-hand panel displays ΔB distribution in the *TS05* model. Due to the lack of cusp currents, the depressions are much weaker, being solely due to the vacuum null points at the magnetopause. Another noteworthy detail is a more realistic equatorial field in the *TS05* model, with a significant depression within $r < 5\ R_E$, a feature virtually missing in the MHD-simulated field.

39.3.4. Hybrid Approach

A common curse and stumbling block of modeling the magnetosphere is the extremely wide range of spatial scales, ranging from tens of kilometers up to several R_E. From the viewpoint of modular approach, the problem is not hopelessly intractable, due to a wide choice of available methods. However, the modular models lack in flexibility and are inevitably restricted by a *priori* assumptions. On the other hand, relying solely on formal RBF/BBF expansions as a universal remedy is also not an option. Indeed, in order to resolve the low-altitude FACs, the grid nodes must densely cover the innermost region $1 \le r \le 3\ R_E$. In such a case, attempts to smoothly extend the fine inner grid to larger distances and construct a global model with a decent resolution would inevitably result in a computationally prohibitive number of the nodes. In addition, data distribution in the fitting samples is often too uneven, both spatially and parametrically. Using the "overflexible" RBF and BBF models in such cases may result in artificial bumpiness of the model field, not to mention the currents.

A natural way out of this dilemma is to synthesize the modular and the RBF/BBF methods. The first step is to derive from data a first-order approximation, composed of contributions from the MP, TC, SRC, PRC, and FAC modules. Once their parameters are evaluated and fixed, the RBF/BBF component of the model is fitted to the residual field, thus minimizing the remaining deviation of the modular component from the data. The RBF/BBF expansions serve in this method as a higher

order correction to the modular part of the model. Such a two-step procedure is at the core of the "hybrid" approach (Tsyganenko and Andreeva, 2017). A graphical illustration of the RBF correction effect is presented in Figure 39.9, whose panels from left to right show scatterplots of three model field components against those in the original data set. The upper row corresponds to the purely modular model, fitted to data without the RBF component, and the bottom panels show the result for the full hybrid model. A dramatic improvement is clearly evident in the much tighter grouping of the data clouds around the main diagonal in the bottom plots, as well as in the higher values of the correlation coefficients. In this example, the "data" **B** vectors were generated by an MHD simulation; in the case of real satellite data, the improvement is somewhat less: typically, the RBF/BBF correction decreases the residual r.m.s. mismatch by ~10%.

Another advantage of the hybrid approach is that, due to the presence of the modular component as a principal contributor to the total $\mathbf{B}_{ext}$ vector, such constructed model fields retain the property of being at least approximately shielded on a global scale. Purely RBF/BBF models are less adequate in that sense, so their best application area is the local magnetic field modeling, such as, e.g., a numerical representation of the geosynchronous magnetic field (Andreeva and Tsyganenko, 2018). Figure 39.10 presents an example of validating such a local model against data of GOES-15 satellite, taken during a storm of 18–21 February 2012.

39.4. PARAMETERIZATION OF THE DATA-BASED MODELS

Due to high variability of the distant geomagnetic field, a model fitted to the entire pool of archived data would represent only an average, mostly quiet magnetosphere. The main goal of the modeling, however, is to describe the magnetospheric dynamics in relatively rare space weather events. The principal difficulty lies, on the one hand, in the large variety of possible disturbance scenarios and in the extreme sparsity of simultaneous real-time spacecraft observations on the other. This is essentially what makes the space weather modeling fundamentally different from the meteorological forecasting, based on the abundant flow of real-time data from thousands of ground stations. In the case of magnetosphere modeling, by contrast, most multipoint information comes from

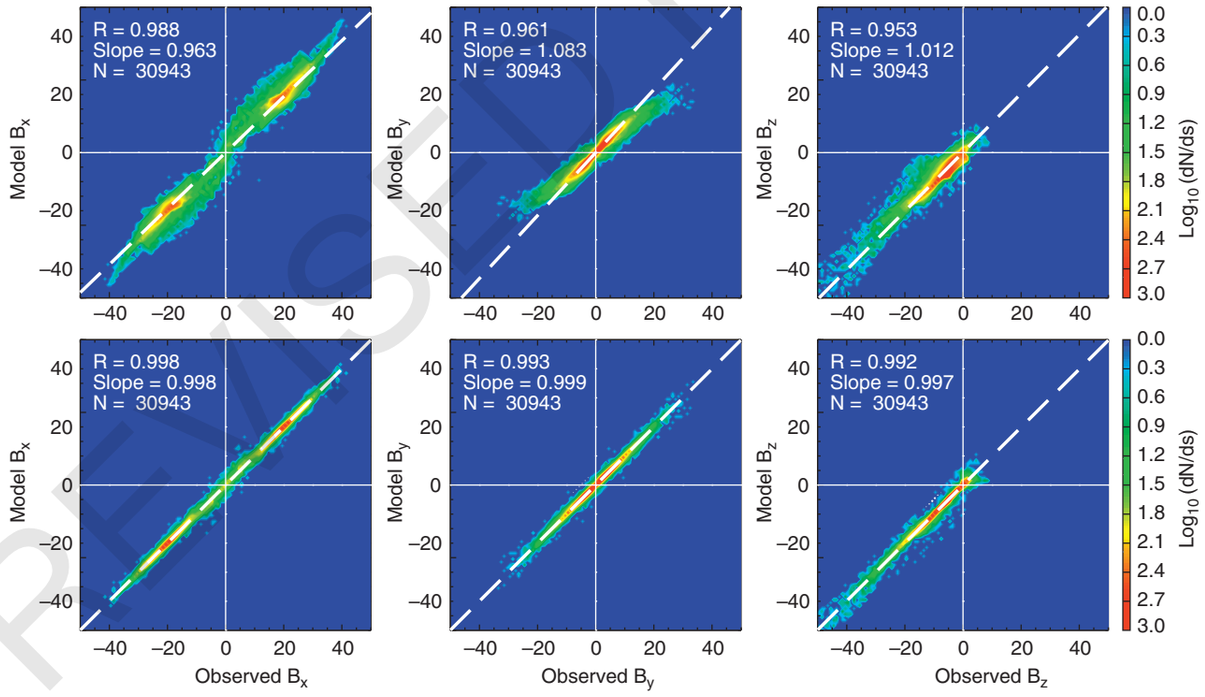

Figure 39.9 Bivariate scatterplots illustrating the effect of combining the modular (*TA15*) and RBF components into a synthetic "hybrid" model. The upper row of panels shows the result of fitting only the TA15 model to a subset of artificial "data" generated in an MHD simulation. The lower row displays similar diagrams but for the full hybrid model field, The color indicates on a logarithmic scale the number dN of data points falling into ds =1nT × 1nT bins of B_x, B_y, B_z.

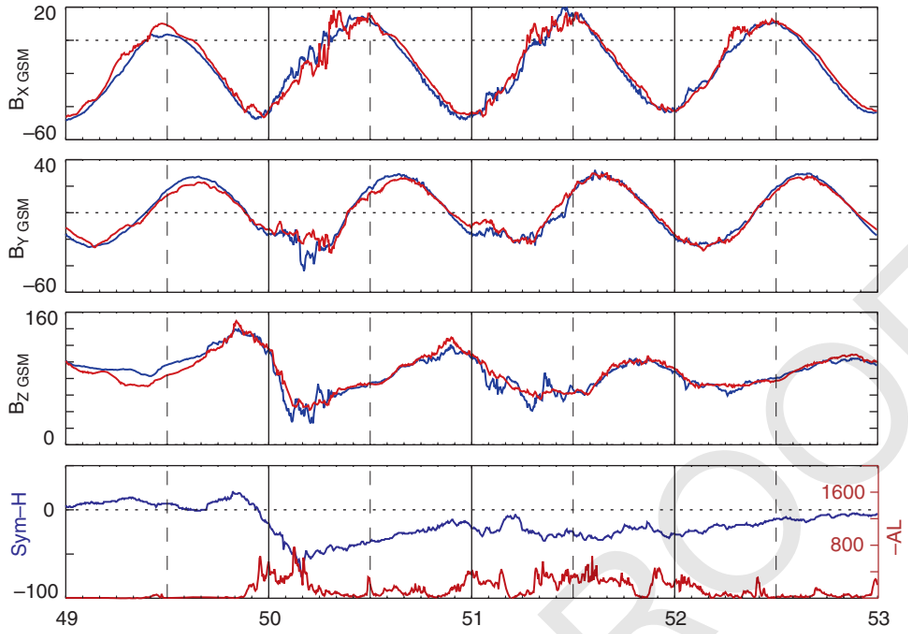

Figure 39.10 Comparing the output of a local geosynchronous field model (red) with GOES 15 data (blue) taken during a moderate storm of 18–21 February 2012. The bottom panel displays the concurrent variation of Sym-H (blue) and -AL indices (after Andreeva and Tsyganenko, 2018).

historical data archives. This brings forward a fundamental paradigm upon which the empirical modeling is based. It lies in the assumption that geomagnetic configurations realized in different events, but with similar patterns of external input and/or in the same range of ground-based indices, are also similar. This postulate serves as the basic justification for using asynchronous (archived) data to reconstruct the magnetosphere in specific events. The assumed determinism is, of course, limited by a host of inherently chaotic processes and instabilities, resulting in a far wider diversity of actual evolution scenarios. Unfortunately and inevitably, all those fluctuations remain beyond our prediction capabilities, even with the fullest knowledge of interplanetary conditions.

39.4.1. Direct Binning and "Climatological" Models

Due to the absence of systematic data from interplanetary monitors in the first decades of the space era, the only way to parameterize the magnetospheric state was to use ground activity indices. The first data-based *MF75* model employed the Kp-index as a measure of the magnetospheric disturbance, and a similar method was used in the following *TU82, T87,* and *T89* models. The data were binned into several subsets corresponding to consecutive intervals of Kp, and the model parameters were separately derived for each data subset. The model field configurations revealed systematic changes due to stronger compression of the magnetosphere and increasingly intense ring and tail currents, associated with growing Kp, as illustrated in Figure 39.11 based on the *T89* model.

The four panels in Figure 39.11 correspond to four Kp intervals, from the most quiet (Kp = 0,0+) to the most disturbed (Kp > 5+), and demonstrate a dramatic stretching of the tail lines, accompanied by increasingly deeper field depression in the inner magnetosphere. On the dayside, one sees a growing compression of the magnetopause and progressive equatorward shift of the polar cusps. Models of this kind represent highly averaged states of the magnetosphere and cannot replicate its dynamics in individual events; for that reason they are referred to as "climatological' models.

39.4.2. Parameterization by the "Dynamical Response" Functions

This approach is best suited for the modular models in which the total field is divided into a few parts associated with main current systems, overviewed in section 39.3.1. First proposed in Tsyganenko and Sitnov (2005), it is based on the premise that the individual magnetospheric field sources respond differently to the interplanetary driving and have different relaxation timescales. It is

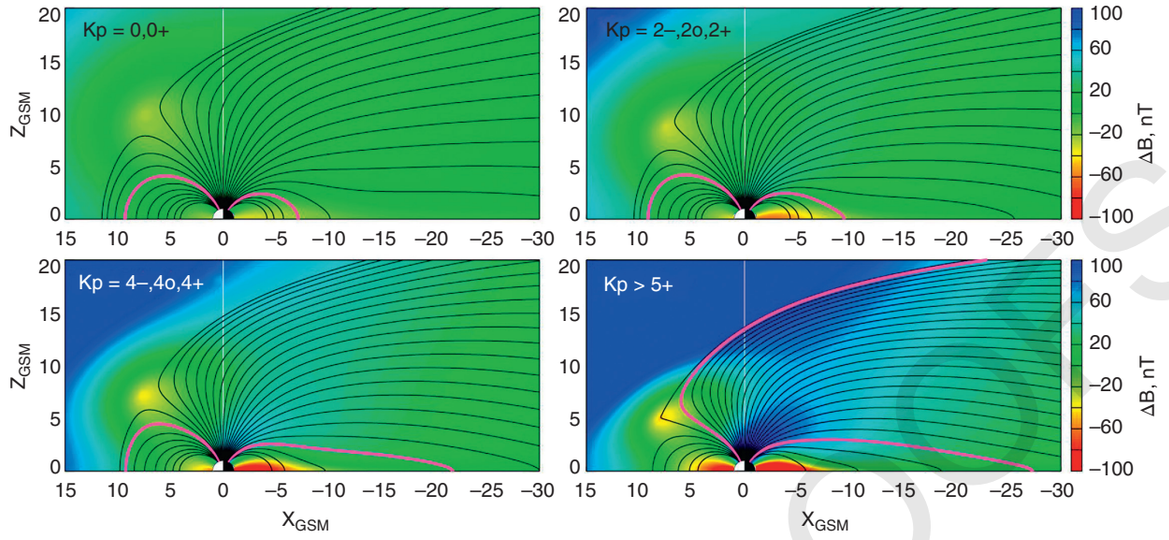

Figure 39.11 Noon–midnight cuts of the model magnetosphere (T89), corresponding to four intervals of the Kp-index. The field lines are plotted at 2° cadence of the footpoint latitude, starting from 60°. To better illustrate the difference in the field line stretching, the nightside and dayside lines with footpoint latitudes 66° and 72°, respectively, are highlighted with magenta. The background color illustrates the field compression (blue) and depression (red), in terms of the scalar difference ΔB between the total model field and that due to only the Earth's dipole,

further assumed that each current system has two modes of response. The first mode is a virtually instantaneous reaction to changes of the solar wind pressure, rapidly propagating inside the magnetosphere via Alfven waves. The second mode is associated with slower processes, such as magnetic flux transport or plasma convection. The external driving is competing with internal losses, which is empirically modeled by including in the module magnitudes of dynamical variables W, derived from the source-loss equation:

$$\frac{dW}{dt} = S(t) - L(W) \tag{39.10}$$

The source term $S(t)$ in the right-hand side defines the growth rate of a current system due to the external driving, whose specific form is sought as an optimal combination of interplanetary parameters. In the *TS05* model, it was assumed in the form $S = aN^{\lambda}V^{\beta}B_s^{\gamma}$, where N, V, and B_s are the solar wind density, speed, and the half-wave rectified southward component of the IMF, respectively, raised to *a priori* unknown exponents λ, β, and γ.

The loss term $L(W)$ represents the relaxation rate of the field source. Its physical interpretation depends on a current system in question: for example, in the case of the RC it corresponds to the loss of particles due to charge exchange, precipitation, drift losses, etc. In the *TS05* model, it was assumed proportional to the difference between the current value of W and its quiet-time level: $L(W) = (W - W_0)/T$. In such a case, equation (39.10) becomes equivalent to the equation by Burton et al. (1975), yielding exponential relaxation of W to its pre-storm level after the external driving is turned off, with the e-folding decay timescale T. This yields a simple solution for each field source in the form:

$$W(t) = W_0 + \int_0^t S(\tau) \exp\frac{\tau - t}{T} d\tau \tag{39.11}$$

where the integration is made from the beginning of the event $\tau = 0$ to the current moment $\tau = t$.

In practice, the continuous integration in equation (39.11) is replaced by discrete summation, with the exponents λ, β, γ, and the relaxation times T separately defined for each field source and treated as unknown parameters to be determined from data. Figure 39.12 (Tsyganenko and Sitnov, 2005), compares the observed variation of the Sym-H index with that predicted by the *TS05* model for a 12-day interval of the long double storm of 3–14 September 2002. The overall agreement is remarkably good in this case.

The six coloured curves show separate contributions to the index from individual current systems, as explained in the caption. In agreement with Alekseev et al. (1996), the principal contribution to the Sym-H/Dst index at the peak of the storm comes not from the SRC alone, as was

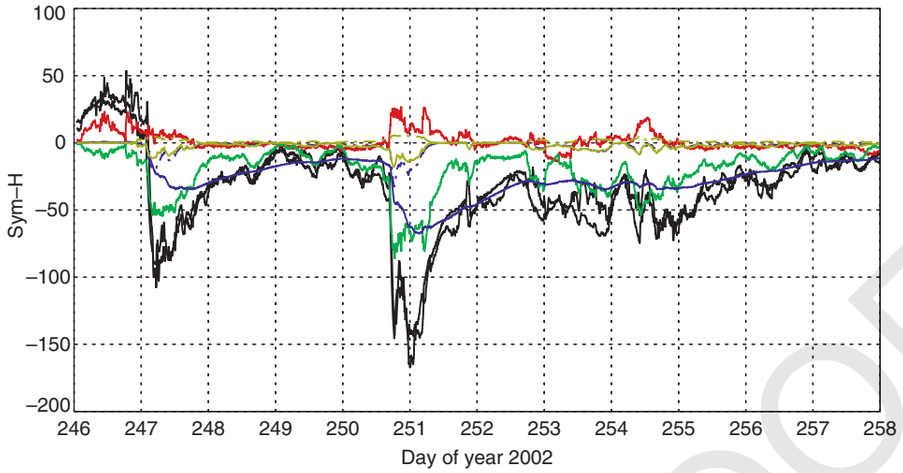

Figure 39.12 Comparison of the observed Sym-H variation (thick black line) with that derived from the *TS05* model (thin black line). Colored lines show individual contributions to the stormtime Sym-H from the major external field sources: TC (green), RC (blue), MP (red).

believed in the early days of space physics, nor solely from the TC, as was argued by Maltsev (2004), but from both these sources in roughly equal shares. However, due to its much shorter relaxation time, the TC contribution decreases during the recovery phase much faster than that of the SRC.

The *TS05* model was fitted to a database compiled from observations during 37 storms between 1996 and 2000, including a few events with the Dst peak below −300 nT. The principal finding was the enormous deformation of the inner magnetosphere during the megastorm peaks, especially pronounced in the dusk sector. The model reproduced the observed dramatic expansion of the auroral oval to unusually low geomagnetic latitudes of 56–58° during extreme events. Regarding the individual field source dynamics, a wide range of the relaxation timescales was found, from a fraction of hour in the case of Region 1 FACs up to ~30 hours for the inner ring current.

39.4.3. "Nearest Neighbor" Data Mining

By the early 2000s, the vastly increased amount of archived magnetospheric and interplanetary data opened an opportunity to devise more advanced parameterization methods. Instead of binning data into intervals of a single disturbance index, Sitnov et al. (2008) proposed to select them by means of a sophisticated search in a multidimensional parameter space. The current state of the magnetosphere is represented in that method by three state variables, which include the sliding averages $\langle \mathrm{Sym-H} \rangle$ and $D\langle \mathrm{Sym-H} \rangle/Dt$, quantifying the current intensity of the field sources and its time derivative, respectively, and the average dawn–dusk component of the interplanetary electric field $\langle vB_z \rangle$ as a third coordinate. Thus defined averages serve as phase space coordinates that determine the state of the magnetosphere and its trend in the unfolding storm process. The solar wind pressure is treated separately: instead of being added as a fourth dimension, it enters in the model via appropriate scaling parameters.

The above parameters, normalized by their standard deviations, are calculated for consecutive time moments, from the beginning to the end of a disturbance event, and form a sequence of vectors in the parametric space of state variables, thus representing the event history. The next step is to define a fixed distance limit D and create a sequence of "nearest neighbor" (NN) subsets, each composed of data that fall into a hypersphere of radius D, gradually moving in the parametric space. Fitting to those subsets a flexible *TS07D* field model (section 39.3.2) makes it possible to reconstruct a dynamic sequence of magnetospheric configurations in the course of specific events (Sitnov et al., 2017, and refs. therein). As shown in the most recent study (Stephens et al., 2019), adding the slide-averaged AL-index and its time derivative as the fourth and fifth coordinates of the parametric hyperspace enables the model to reproduce substorm effects, which so far remained beyond the reach of the empirical models.

Figure 39.13 displays *a* 3-D visualization of the equatorial currents and R2 FACs as reconstructed by the NN model near the minimum of the pressure corrected Sym-H index for a March 2013 geomagnetic storm (day 17/DOY 76, UT 12:00). The electric current flow lines are drawn for every nine degrees of footpoint longitude, with white/black color indicating downward/upward

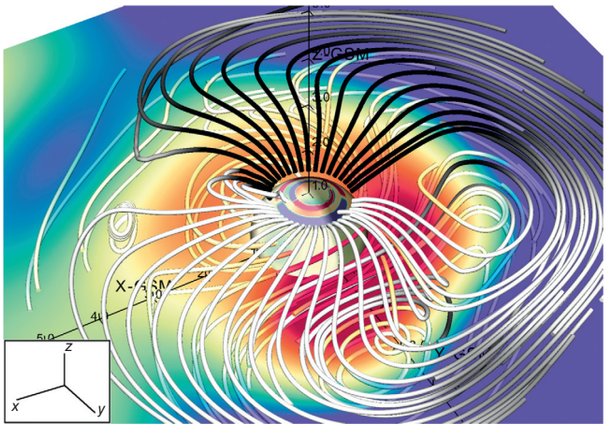

Figure 39.13 A 3-D visualization of electric currents as reconstructed by the nearest neighbor *TS07D* model (Stephens et al., 2019, reproduced with permission of John Wiley & Sons) for the main phase peak of the 17 March 2013 magnetic storm. For the sake of clarity, only the northern part of the configuration is displayed. See text for details.

currents. The FAC polarity at ionospheric level is also indicated, with downward/upward FACs shown in blue/red. The near-equatorial currents are also drawn, illustrating the low-latitude structure of the entire system. The figure demonstrates the model's ability to resolve both westward and eastward parts of the PRC, as well as their connection in the form of "horseshoe" or "banana" currents (Roelof et al., 2004; Liemohn et al., 2013).

The efficiency of the NN approach depends on several factors. First, the state variables must include the ground-based and/or interplanetary parameters in optimal combinations, best reflecting their geoeffectivity. Second, in order to accurately discriminate the data belonging to essentially different magnetospheric states, the number of state variables (i.e., dimensionality of the parameter space) should not be too small, and the variables should be independent of each other, to minimize interplay effects. At the same time, it should be realized that adding more state variables rapidly decreases the number of data points falling in individual subsets, so that an optimal trade-off must be found. In the NN-based modeling, a typical number of records in a subset is in the order of a few thousand; by contrast, in the statistical approach based on dynamical response variables (section 39.4.2), that number varies from tens to hundreds of thousands. At the opposite end of this hierarchy are the adaptive models, addressed in the next section.

39.4.4. Adaptive Modeling

All the models discussed above are essentially based on observations made at different times. Thus, however sophisticated the driving/response algorithm or however accurate the NN selection procedure, the modeling results may tangibly deviate from actual observations. An interesting question is, then, whether one can locally reconstruct an instantaneous magnetic configuration using the simultaneous data of only a few satellites, with the rest of the information provided by a statistical model driven by concurrent interplanetary and/or ground data. This idea is at the core of the adaptive, or event-oriented, approach, conceived in late 1980s. Pulkkinen (1991) modeled the substorm growth phase via an *ad hoc* adjustment of the intensity and thickness of the *T89* TC sheet. A typical problem in this approach is too small a number of data points to unambiguously derive unknown parameters. As an effective remedy (Kubyshkina et al., 1999, 2009) suggested constraining the models with additional data, such as the plasma pressure and low-altitude position of particle isotropy boundaries.

Figure 39.14 shows a result of the *AM03* adaptive modeling (Kubyshkina et al., 2011) based on data taken by THEMIS and GOES-11 satellites during an hour-long interval 04:00–05:00 UT on 15 March 2009. The diagrams A–D, G–H compare absolute magnitudes of the observed external field $|\mathbf{B}|_{ext}$ (black) with output of the adapted AM03 model (red) and uncorrected T96 (blue). A significant improvement of the fit is clearly seen in all cases. An even better fit is achieved in the values of the equivalent lobe field (panels B–D), calculated for more distant THEMIS 1 and 2 probes by adding the observed plasma and magnetic pressures.One should be aware though of the inherently local nature of the adaptive models. Based on data from a small number of probes, unevenly spaced within a limited range of distance and longitude, they are unlikely to realistically extrapolate the obtained configurations outside the spatially restricted modeling region. A natural solution to the problem is to expand a handful of space probes into a large constellation of many satellites, a subject of the next, concluding section.

39.5. FUTURE PROSPECTS AND CHALLENGES: CONSTELLATION-DATA BASED MODELS

Notwithstanding the remarkable progress of MHD and particle simulations, the spacecraft observations are and will remain the basis of the magnetospheric and space weather studies. In the future, one can envision the data being collected by a large constellation of small satellites, continuously and simultaneously monitoring the geospace and the incoming solar wind. The uninterrupted flow of in *situ* data will be used as a periodic correcting input to the first-principle simulation runs, in the same way as the meteorological data are now routinely

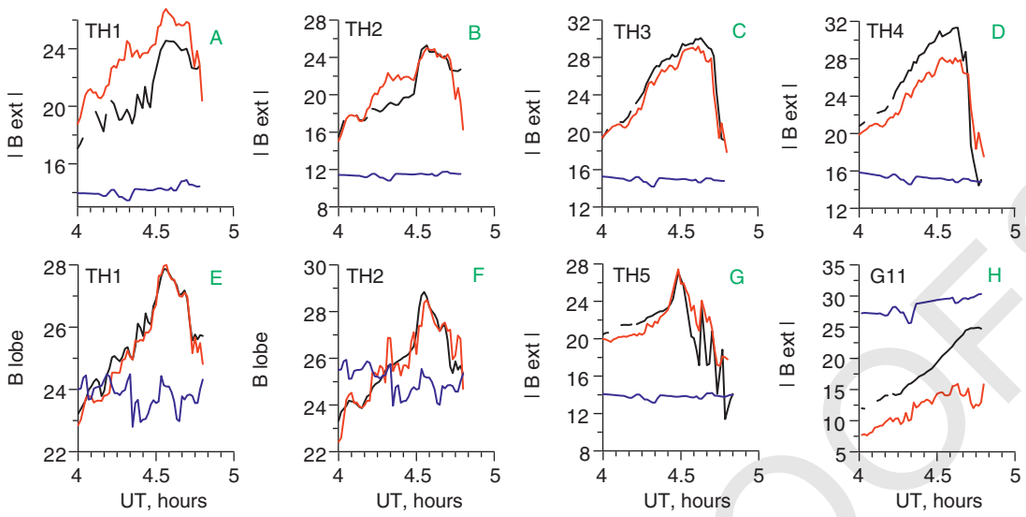

Figure 39.14 Illustrating the adaptive reconstruction of the magnetic field for the interval 4–5 UT of 15 March 2009. Panels A–D, G–H compare variations of the observed (black), original *T96* (blue), and adapted *AM03* external field magnitude at locations of THEMIS 1–5 and GOES 11 satellites. Panels E and F show in the same format variations of the equivalent lobe field at distances corresponding to THEMIS 1 and 2 locations in the plasma sheet.

assimilated into computations of the global atmospheric circulation. The main difference and the principal problem here is that, unlike the ground weather stations, the moving satellites cannot form a spatially fixed monitoring system, but continuously change their positions. Assimilating the space weather data can be greatly facilitated with the use of data-based models, driven by the concurrent data from interplanetary monitors and adjusted by fitting them to the real-time constellation data. First numerical experiments in that direction, based on then available *T96* model, were described two decades ago (Tsyganenko, 1998b). The principal challenge here is to derive from the data reasonably accurate model configurations, in spite of the inevitable highly variable spatial unevenness of the data sources.

A reasonable strategy for the real-time reconstruction of the magnetospheric configuration can be envisaged as an iterative two-step procedure. In the first step, an approximate distribution of the magnetic field is obtained, based on an empirical forecasting model fed with real-time interplanetary data from the constellation satellites in the upstream solar wind. In the second step, the initial model configuration is corrected using the data from the intramagnetospheric part of the space probe constellation, either solely on the basis of the same modular model, or by adding a higher resolution component like the above described system of RBF/BBF sources. Of crucial importance here is the regularity of the reconstructed field in the areas devoid of data. This issue will require extensive analysis and numerical experiments, including, in particular, the use of regularization methods for underdetermined/overfitted problems (Gershenfeld, 2003 (Chapter 12); Connerney, 1981; Moore et al., 2017). Finally, it should be noted that the biggest challenge of this attractive project is of technological nature, which is to launch and maintain an optimally configured constellation of minisatellites capable of providing a continuous flow of reliable data.

ACKNOWLEDGMENTS

The research at the University of Saint-Petersburg was supported by the Russian Science Foundation grant 14-17-00072, as well as the Russian Foundation for Basic Research grants 17-05-00415 and 20-05-00218. The JHU/APL coauthors acknowledge the National Science Foundation grant AGS-1702147 and the National Aeronautics and Space Administration grant NNX16AB78G.

REFERENCES

Akasofu, S.-I., and S. Chapman(1961), The ring current, geomagnetic disturbance, and the Van Allen radiation belts, *J. Geophys. Res.*, 66, 1321–1350.

Alekseev, I. I., and V. P. Shabansky (1972), A model of the magnetic field in the geomagneto-sphere, *Planet. Space Sci.*, 20, 117–133.

Alekseev, I. I., E. S. Belenkaya, V. V. Kalegaev, Y. I. Feldstein, and A. Grafe (1996), Magnetic storms and magnetotail currents, *J. Geophys. Res.*, 101, 7737–7751.

Andreeva, V. A., and N. A. Tsyganenko (2016), Reconstructing the magnetosphere from data using radial basis functions,

J. Geophys. Res.: Space Phys., 121, 2249–2263, doi:10.1002/2015JA022242.

Andreeva, V. A., and N. A. Tsyganenko (2018), Empirical modeling of the quiet and storm time geosynchronous magnetic field, *Space Weather*, 16, 16–36, https://doi.org/10.1002/2017SW001684.

Burton, R. K., R. L. McPherron, and C. T. Russell (1975), An empirical relationship between interplanetary conditions and Dst, *J. Geophys. Res.*, 80, 4204–4214.

Connerney, J. E. P. (1981), The magnetic field of Jupiter: A generalized inverse approach, *J. Geophys. Res.*, 86, 7679–7693.

Fairfield, D. H., N. A. Tsyganenko, A. V. Usmanov, and M. V. Malkov (1994), A large magnetosphere magnetic field database, *J. Geophys. Res.: Space Phys.*, 99, 11319–11326.

Gershenfeld, N. (2003). *The nature of mathematical modeling*. Cambridge University Press, Cambridge. ISBN 0-521-57095-6.

Iijima, T., and T. A. Potemra (1976), The amplitude distribution of field-aligned currents at northern high latitudes observed by Triad, *J. Geophys. Res.*, 81, 2165–2174.

Korth, H., B. J. Anderson, and C. L. Waters (2010), Statistical analysis of the dependence of large-scale Birkeland currents on solar wind parameters, *Ann. Geophys.*, 28, 515–530.

Korth, H., L. Rastaetter, B. J. Anderson, and A. J. Ridley (2011), Comparison of the observed dependence of large-scale Birkeland currents on solar wind parameters with that obtained from global simulations, *Ann. Geophys.*, 29, 1809–1826.

Kosik, J.-C. (1989), Quantitative magnetic field model including magnetospheric ring current, *J. Geophys. Res.: Space Phys.*, 94(A9), 12021–12026.

Pulkkinen, T. I. (1991), A study of magnetic field and current configurations in the magnetotail at time of a substorm onset. *Planet. Space Sci.*, 39, 883–845.

Kubyshkina, M. V., V. A. Sergeev, and T. I. Pulkkinen (1999), Hybrid input algorithm: An event-oriented magnetospheric model, *J. Geophys. Res.*, 104, 24977–24993.

Kubyshkina, M., V. Sergeev, N. Tsyganenko, V. Angelopoulos, A. Runov, H. Singer, et al. (2009), Toward adapted time-dependent magnetospheric models: A simple approach based on tuning the standard model, *J. Geophys. Res.,* 114, A00C21, doi:10.1029/2008JA013547.

Kubyshkina, M., V. Sergeev, N. Tsyganenko, V. Angelopoulos, A. Runov, E. Donovan, et al. (2011), Time-dependent magnetospheric configuration and breakup mapping during a substorm, *J. Geophys. Res. Space Phys.,* 116, A00I27, doi:10.1029/2010JA015882.

Laundal, K. M., C. C. Finlay, N. Olsen, and J. P. Reistad (2018). Solar wind and seasonal influence on ionospheric currents from Swarm and CHAMP measurements. *J. Geophys. Res.: Space Phys.*, 123, 4402–4429, https://doi.org/10.1029/2018JA025387.

Liemohn, M. W., N. Y. Ganushkina, R. M. Katus, D. L. De Zeeuw, and D. T. Welling (2013), The magnetospheric banana current, *J. Geophys. Res.: Space Phys.*, 118, 1009–1021, doi:10.1002/jgra.50153.

Lin, R. L., X. X. Zhang, S. Q. Liu, Y. L. Wang, and J. C. Gong (2010), A three-dimensional asymmetric magnetopause model, *J. Geophys. Res.: Space Phys.,* 115, A04207, doi:10.1029/2009JA014235.

Lui, A. T. Y., and D. C. Hamilton (1992), Radial profiles of quiet time magnetospheric parameters, *J. Geophys. Res.*, 97(A12), 19325–19332, doi:10.1029/92JA01539.

Mailyan, B., C. Munteanu, and S. Haaland (2008), What is the best method to calculate the solar wind propagation delay? *Ann. Geophys.*, 26, 2383–2394.

Maltsev, Y. P. (2004), Points of controversy in the study of magnetic storms, *Space Sci. Rev.*, 110, 227–267.

Mead, G. D., and D. B. Beard (1964), Shape of the geomagnetic field solar wind boundary, *J. Geophys. Res.*, 69, 1169–1170.

Mead, G. D., and D. H. Fairfield (1975), A quantitative magnetospheric model derived from spacecraft magnetometer data, *J. Geophys. Res.*, 80, 523–534.

Moore, K. M., J. Bloxham, J. E. P. Connerney, J. L. Jorgensen, and J. M. G. Merayo (2017), The analysis of initial Juno magnetometer data using a sparse magnetic field representation, *Geophys. Res. Lett.*, 44, 4687–4693, doi:10.1002/2017GL073133.

Newell, P. T., T. Sotirelis, K. Liou, C.-I. Meng, and F. J. Rich (2007), A nearly universal solar wind–magnetosphere coupling function inferred from 10 magnetospheric state variables, *J. Geophys. Res.: Space Phys.,* 112, A01206, doi:10.1029/2006JA012015.

Olson, W. P., and K. A. Pfitzer (1974), A quantitative model of the magnetospheric magnetic field, *J. Geophys. Res.: Space Phys.*, 79(25), 3739–3748.

Ostapenko, A. A., and Y. P. Maltsev (1997), Relation of the magnetic field in the magnetosphere to the geomagnetic and solar wind activity, *J. Geophys. Res.: Space Phys.*, 102(A8), 17467–17473.

Roederer, J. G. (1969), Quantitative models of the magnetosphere, *Rev. Geophys.*, 7(1, 2), 77–96.

Roelof, E. C. (1989), Remote sensing of the ring current using energetic neutral atoms, *Adv. Space Res.*, 9(12), 12195–12203.

Roelof, E. C., P. C. Brandt, and D. G. Mitchell (2004), Derivation of currents and diamagnetic effects from global plasma pressure distributions obtained by IMAGE/HENA, *Adv. Space Res.*, 33, 747–751.

Rossi, B., and S. Olbert (1970), *Introduction to the physics of space*, McGraw-Hill, New York.

Schulz, M., and M. C. McNab (1987), Source-surface model of the magnetosphere, *Geophys. Res. Lett.*, 14, 182–185.

Shue, J.-H., P. Song, C. T. Russell, J. T. Steinberg, J. K. Chao, G. Zastenker, O. L. Vaisberg, S. Kokubun, H. J. Singer, T. R. Detman, and H. Kawano (1998), Magnetopause location under extreme solar wind conditions, *J. Geophys. Res.: Space Phys.,* 103(A8), 17,691–17,700.

Sitnov, M. I., N. A. Tsyganenko, A. Y. Ukhorskiy, and P. C. Brandt (2008), Dynamical data-based modeling of the storm-time geomagnetic field with enhanced spatial resolution, *J. Geophys. Res.: Space Phys.,* 113, A07218, doi:10.1029/2007JA013003.

Sitnov, M. I., N. A. Tsyganenko, A. Y. Ukhorskiy, B. J. Anderson, H. Korth, A. T. Y. Lui, and P. C. Brandt (2010), Empirical modeling of a CIR-driven magnetic storm, *J. Geophys. Res.: Space Phys.,* 115, A07231, doi:10.1029/2009JA015169.

Sitnov, M. I., G. K. Stephens, N. A. Tsyganenko, A. Y. Ukhorskiy, S. Wing, H. Korth, and B. J. Anderson (2017), Spatial structure and asymmetries of magnetospheric currents inferred from high-resolution empirical geomagnetic field models. In S. Haaland, A. Runov, and C. Forsyth (Eds.), *Dawn-dusk asymmetries in planetary plasma environments, Geophysical Monograph Series* (Vol. 230, pp. 199–212). American Geophysical Union.

Sitnov, M. I., G. K. Stephens, M. Gkioulidou, V. Merkin, A. Y. Ukhorskiy, H. Korth, et al. (2018), Empirical modeling of extreme events: Storm-time geomagnetic field, electric current, and pressure distributions. In N. Buzulukova (Ed.), *Extreme events in geospace: Origins, predictability, and consequences (pp259–279). Elsevier*. https://doi.org/10.1016/B978-0-12-812700-1.00011-X.

Stephens, G. K., M. I. Sitnov, J. Kissinger, N. A. Tsyganenko, R. L. McPherron, H. Korth, and B. J. Anderson (2013), Empirical reconstruction of storm time steady magnetospheric convection events, *J. Geophys. Res.: Space Phys.*, 118, 6434–6456, doi:10.1002/jgra.50592.

Stephens, G. K., M. I. Sitnov, A. Y. Ukhorskiy, E. C. Roelof, N. A. Tsyganenko, and G. Le, (2016), Empirical modeling of the storm time innermost magnetosphere using Van Allen Probes and THEMIS data: Eastward and banana currents, *J. Geophys. Res.: Space Phys.*, 121, 157–170, doi:10.1002/2015JA021700.

Stephens, G. K., M. I. Sitnov, H. Korth, N. A. Tsyganenko, S. Ohtani, M. Gkioulidou, and A. Y. Ukhorskiy (2019), Global empirical picture of magnetospheric substorms inferred from multi-mission magnetometer data, *J. Geophys. Res.: Space Phys.*, 124*(2),* 1085–1110.

Stern, D. P. (1985), Parabolic harmonics in magnetospheric modeling: The main dipole and the ring current, *J. Geophys. Res.*, 90, 10851–10863.

Stern, D. P. (1987), Tail modeling in a stretched magnetosphere 1. Methods and transformations, *J. Geophys. Res.: Space Phys.*, 92, 4437–4448.

Stern, D. P. (1993), A simple model of Birkeland currents, *J. Geophys. Res:. Space Phys.*, 98, 5691–5706.

Tenfjord, P., N. Ostgaard, K. Snekvik, K. M. Laundal, J. P. Reistad, S. Haaland, and S. E. Milan (2015), How the IMF By induces a By component in the closed magnetosphere and how it leads to asymmetric currents and convection patterns in the two hemispheres, *J. Geophys. Res.: Space Phys.*, 120, 9368–9384, doi:10.1002/2015JA021579.

Thébault, E., C. C. Finlay, C. D. Beggan, et al. (2015), International Geomagnetic Reference Field: the 12th generation, *Earth, Planets Space*, 67, 79, doi:10.1186/s40623-015-0228-9.

Tsyganenko, N. A. (1987), Global quantitative models of the geomagnetic field in the cislunar magnetosphere for different disturbance levels, *Planet. Space Sci.*, 35, 1347–1358.

Tsyganenko, N. A. (1989a), A magnetospheric magnetic field model with the warped tail current sheet, *Planet. Space Sci.*, 37, 5–20.

Tsyganenko, N. A. (1989b), A solution of the Chapman-Ferraro problem for an ellipsoidal magnetopause, *Planet. Space Sci.*, 37, 1037–1046.

Tsyganenko, N. A. (1991), Methods for quantitative modeling of the magnetic field from Birke-land currents, *Planet. Space Sci.*, 39, 641–654.

Tsyganenko, N. A. (1993), A global analytical representation of the magnetic field produced by the Region 2 Birkeland currents and the partial ring current, *J. Geophys. Res.: Space Phys.*, 98, 5677–5690.

Tsyganenko, N. A. (1995), Modeling the Earth's magnetospheric magnetic field confined within a realistic magnetopause, *J. Geophys. Res.: Space Phys.*, 100, 5599–5612.

Tsyganenko, N. A. (1996), Effects of the solar wind conditions on the global magnetospheric configuration as deduced from data-based field models. In E. J. Rolfe and B. Kaldeich (Eds.), *International conference on substorms, Proceedings of the 3rd International Conference* (pp. 181–185). *Publication ESA SP-389, European Space Agency*.

Tsyganenko, N. A. (1998a), Modeling of twisted/warped magnetospheric configurations using the general deformation method, *J. Geophys. Res.: Space Phys.*, 103(A10), 23551–23563.

Tsyganenko, N. A. (1998b), Toward real-time magnetospheric mapping based on multi-probe space magnetometer data. In V. Angelopoulos and P. V. Panetta (Eds.), *Science closure and enabling technologies for constellation class missions* (pp. 84–90). UCLA, Berkeley, CA.

Tsyganenko, N. A. (2000), Modeling the inner magnetosphere: The asymmetric ring current and Region 2 Birkeland currents revisited, *J. Geophys. Res.: Space Phys.*, 105(A12), 27739–27754.

Tsyganenko, N. A. (2002a), A model of the near magnetosphere with a dawn-dusk asymmetry: 1. Mathematical structure, *J. Geophys. Res.: Space Phys.,* 107*(*A8*),* doi:10.1029/2001JA000219.

Tsyganenko, N. A. (2002b), A model of the near magnetosphere with a dawn-dusk asymmetry: 2. Parameterization and fitting to observations, *J. Geophys. Res.: Space Phys.,* 107(A8), doi:10.1029/2001JA000220.

Tsyganenko, N. A. (2009), Magnetic field and electric currents in the vicinity of polar cusps as inferred from Polar and Cluster data, *Ann. Geophys.*, 27, 1573–1582, doi:10.5194/angeo-27-1573-2009.

Tsyganenko, N. A. (2013), Data-based modelling of the Earth's dynamic magnetosphere: a review, *Ann. Geophys.*, 31, 1745–1772, doi:10.5194/angeo-31-1745-2013.

Tsyganenko, N. A. (2014), Data-based modeling of the geomagnetosphere with an IMF-dependent magnetopause, *J. Geophys. Res.: Space Phys.*, 119, 335–354, doi:10.1002/2013JA019346.

Tsyganenko, N. A., and V. A. Andreeva (2015), A forecasting model of the magnetosphere driven by an optimal solar wind coupling function, *J. Geophys. Res.: Space Phys.,* 120, 8401–8425, doi:10.1002/2015JA021641.

Tsyganenko, N. A., and V. A. Andreeva (2016), An empirical RBF model of the magnetosphere parameterized by interplanetary and ground-based drivers, *J. Geophys. Res.: Space Phys.*, 121, 10786–10802, doi:10.1002/2016JA023217.

Tsyganenko, N. A., and V. A. Andreeva (2017), A hybrid approach to empirical magnetosphere modeling, *J. Geophys. Res.: Space Phys.*, 122, 8198–8213, doi:10.1002/2017JA024359.

Tsyganenko, N. A., and V. A. Andreeva (2018a), Building the magnetosphere from magnetic bubbles, *Geophys. Res. Lett.*, 45, 6382–6389, https://doi.org/10.1029/2018GL078714.

Tsyganenko, N. A., and V. A. Andreeva (2018b), Empirical modeling of dayside magnetic structures associated with polar cusps, *J. Geophys. Res.: Space Phys.,* 123, 9078–9092, https://doi.org/10.1029/2018JA025881.

Tsyganenko, N. A., and M. Peredo (1994), Analytical models of the magnetic field of diskshaped current sheets, *J. Geophys. Res. Space Phys.*, 99, 199–205.

Tsyganenko, N. A., and C. T. Russell (1999), Magnetic signatures of the distant polar cusps: Observations by Polar and quantitative modeling, *J. Geophys. Res.: Space Phys.*, 104, 24939–24955.

Tsyganenko, N. A., and M. I. Sitnov (2005), Modeling the dynamics of the inner magnetosphere during strong geomagnetic storms, *J. Geophys. Res. Space Phys.,* 110(A3), A03208, doi:10.1029/2004JA010798.

Tsyganenko, N. A., and M. I. Sitnov (2007), Magnetospheric configurations from a high-resolution data-based magnetic field model, *J. Geophys. Res.: Space Phys.,* 112, A06225, doi:10.1029/2007JA012260.

Tsyganenko, N. A., and D. P. Stern (1996), Modeling the global magnetic field of the large-scale Birkeland current systems, *J. Geophys. Res.: Space Phys.*, 101, 27187–27198.

Tsyganenko, N. A., and A. V. Usmanov (1982), Determination of the magnetospheric current system parameters and development of experimental geomagnetic field models based on data from IMP and HEOS satellites, *Planet. Space Sci.*, 30, 985–998.

Tsyganenko, N. A., S. B. P. Karlsson, S. Kokubun, T. Yamamoto, A. J. Lazarus, K. W. Ogilvie, et al. (1998), Global configuration of the magnetotail current sheet as derived from Geotail, Wind, IMP 8, and ISEE 1/2 data, *J. Geophys. Res.*, 103, 6827–6841.

Voigt, G.-H. (1973), A three dimensional analytical magnetospheric model with defined magnetopause, *J. Geophys.*, 38, 319–346.

Wolf-Gladrow, D. (1987), An introduction to poloidal and toroidal fields, *Mitt. Inst. Geophys. Meteorol. Univ. Koeln*, 54, 1–12.

Zmuda, A. J., and J. C. Armstrong (1974), The diurnal flow pattern of field-aligned currents, *J. Geophys. Res.*, 79, 4611–4619.